Materials Advances

ROYAL SOCIETY OF CHEMISTRY

PAPER

View Article Online
View Journal | View Issue

Cite this: *Mater. Adv.*, 2025, **6**, 6956

Size and surface properties of polydopamine nanoparticles tunable *via* controlled oxidation conditions

Antonello Nucera, [a] Rita Guzzi, [ba] Giovanni Desiderio,[a] Antonio Ferraro,[a] Giovanni Dal Poggetto,[c] Marco Castriota[ba] and Oriella Gennari *[a]

Polydopamine nanoparticles (PDA NPs) have emerged as a versatile biomimetic material with tunable physicochemical properties, making them promising candidates for applications in biomedicine, energy storage, and photothermal therapy. In this study, we investigate the structural and functional evolution of PDA NPs synthesized under controlled oxidation conditions, emphasizing the interplay between molecular crosslinking, surface roughness, and optical properties. A systematic analysis using SEM, FTIR, and Raman spectroscopy reveals a progressive transformation of catechol (–OH) groups into quinones, leading to increased π–π stacking and crosslinking, which modulates both electronic and photothermal behaviour. Dynamic light scattering (DLS) analysis identified 24 hours as the optimal synthesis window, yielding uniform and colloidally stable nanoparticles ($D_H \approx 154$ nm; ζ-potential ≈ −41 mV). At early oxidation stages (1–24 h), the high availability of free catechol and amine groups supports enhanced electron delocalization, while at intermediate oxidation times (48 h), excessive crosslinking restricts charge mobility, limiting functional performance. Prolonged oxidation (96–120 h) results in increased roughness, influencing both light absorption and heat diffusion. Comparative photothermal analysis with *Sepia melanin* demonstrates that PDA NPs exceed the thermal performance of natural eumelanin in both tunability and photothermal conversion efficiency, reaching a $\Delta T \approx 48.9$ °C, for the 120 h oxidation NPs. The findings highlight the critical role of oxidation-driven molecular modifications in defining PDA's optical and thermal performance. These insights establish a structure–property framework for optimizing PDA NPs for life science applications.

Received 14th April 2025,
Accepted 25th August 2025

DOI: 10.1039/d5ma00359h

rsc.li/materials-advances

1. Introduction

The possibility to customize nanostructures, especially nanoparticles (NPs), is of great relevance in many innovative applications, primarily due to their peculiar physical and chemical properties, such as mechanical, thermal, magnetic, electronic, optical, and catalytic, compared to bulk material.[1] In nanomedicine and biomedical applications, controlling nanoparticle size is essential, as it influences circulation, biodistribution, and clearance, directing NPs to specific biological targets.[1–3] Additionally, NP shape affects internalization and drug release processes, determining the degree of accumulation at target sites.[1]

The development of stable and efficient nanoparticles relies on monodispersity and precise size control, which are critical for ensuring reproducible performance across applications.[4] Moreover, the chemical composition of nanoparticles governs their functional behavior and consequently determines their suitability for specific application fields. Organic nanoparticles, including polydopamine (PDA),[5,6] are particularly advantageous due to their sensitivity to heat and light, enabling applications in cancer therapy[7] and drug delivery.[8–10] Their unique electrical conductivity also makes them ideal for bioimaging,[11] tissue engineering,[12] and sensing applications.[13–15] Among organic nanoparticles, PDA is one of the most extensively investigated melanin-inspired materials due to its radical-scavenging properties,[16–18] photothermal conversion efficiency,[19–21] and antioxidant activity.[22] PDA-based materials have been widely explored for surface coatings,[23,24] polymeric materials,[25] quantum dots, and 3D nanoparticles. Furthermore, their biocompatibility, biodegradability,[26] drug-loading capacity,[27] and tunable photothermal efficiency[19,20,28] make them highly attractive for biomedical applications.[29,30]

PDA NPs are synthesized through the oxidative self-polymerization of dopamine monomers in alkaline solutions.[19,27]

[a] *Institute of Nanotechnology, CNR-NANOTEC, 87036 Rende (CS), Italy. E-mail: oriella.gennari@cnr.it*
[b] *Department of Physics, University of Calabria, 87036 Rende (CS), Italy*
[c] *Institute of Polymers, Composites and Biomaterials, IPCB-CNR, Via Campi Flegrei 35, 80078, Pozzuoli (NA), Italy*

Despite extensive research, achieving tunable control over oxidation-induced crosslinking and surface modifications remains a major challenge, impacting their photothermal and biomedical applications. To address this, novel synthetic approaches are being developed to regulate PDA NP size and morphology.

This study systematically examines the growth kinetics of PDA NPs under oxidative polymerization in alkaline media, achieving precise size and uniformity control by adjusting oxidant concentration and reaction time. We utilize Scanning Electron Microscopy (SEM) and Transmission Electron Microscopy (TEM) for morphological characterization and Fourier-transform infrared (FTIR) and Raman spectroscopy for structural analysis. Furthermore, we evaluate photothermal conversion efficiency across different oxidative states, revealing a direct relationship between physicochemical properties and functional performance. Our findings underscore the potential of tailored PDA nanoparticles for advanced applications in biomedicine,[31] catalysis,[30] energy storage, and sensing technologies.[32]

2. Experimental section

2.1. Chemicals

Dopamine hydrochloride was purchased by Merck. Ethanol, 2-propanol and ammonium hydroxide (30–33%) were from Sigma-Aldrich. High-purity water (Milli-Q) used in all experiments was obtained from a Millipore Milli-Q purification system. All reagents and solvents were analytical grade.

2.2. Preparation of PDA nanoparticles

The PDA NPs were prepared *via* an oxidative self-polymerization process of monomer in an alkaline solution.[19] Firstly, a solution was prepared mixing 4 mL of ethanol and 9 mL of water; NH_4OH was added to obtain initial concentrations of 0.056%, 0.11%, 0.22%, 0.45%, 0.89%, 1.79% and 3.58% (v/v); the solution, as prepared, was stirred, followed by the addition of 50 mg dopamine hydrochloride. The reaction was then allowed to proceed for 24 hours under continuous magnetic stirring. In the case of 1.79% of NH_4OH, the reaction was monitored for over 120 h.

When the reaction was completed, the supernatant was removed by centrifugation (Z 327 K, Hermle LaborTechnik, Wehingen, Germany) at 14 000 rpm for 30 min, and the obtained precipitate was washed, at least four times, with ultrapure water to remove any residues of unreacted monomer and reaction solvent. In all cases, the black pellet obtained was lyophilized using a FreeZone 2.5 Liter Benchtop Freeze Dryer (Labconco Corporation, Kansas City, MO) and used for structural characterization.

2.3. Isolation and characterization of Sepia melanin from *Sepia* ink

Sepia melanin (SM) was extracted from the ink sacs of *Sepia officinalis*, diluted in distilled water, and centrifuged at 14 000 rpm for 30 minutes Sepia melanin (SM) was extracted from the ink sac of *Sepia officinalis*, diluted with water and centrifugated at 14 000 rpm for 30 min. After several washing procedures and redispersion in water, a dispersed solution of clean SM was obtained. The solid mass was lyophilized for 24 h to yield dry powder of SM.

Scanning electron microscopy (SEM), transmission electron microscopy (TEM) and FTIR spectroscopic analysis were performed to characterize morphology and structure of SM.

2.4. Characterization of NPs

2.4.1. Scanning electron microscopy. The morphological properties of PDA NPs were performed using a Scanning Electron Microscopy (Quanta FEG 400F, Fei Company, USA). Before the experiment, each sample was fixed on an aluminum specimen holder with carbon tape and coated with graphite by sputtering process.

The experimental conditions were high vacuum, 15 KV electron acceleration voltage, and secondary electron mode.

2.4.2. DLS analysis. The hydrodynamic diameter (D_H), polydispersity index (PdI), and zeta potential (ζ) of PDA NPs were measured using a Zetasizer Nano ZS (Malvern Instruments Ltd). Data are presented as the mean ± standard deviation (SD) from three independent measurements across two separate batches. Aliquots (800 μL) were collected at defined time points during the 120 h reaction and analyzed immediately.

2.4.3. FTIR spectroscopy and optical properties. PDA NPs produced after 1 h and 24 h, at 1.79% and 3.58% of NH_4OH were analysed by FTIR spectroscopy. SM was used as control/comparison. Samples were dispersed in KBr (99%) and pressed into pellets. The spectra were collected at room temperature from 4000 to 400 cm^{-1} with a resolution of 4 cm^{-1} using a Tensor II FTIR spectrometer (Bruker Optics, Germany). Each spectrum was averaged on 32 scans and up to three replicates were recorded on independent samples to assess reproducibility. Acquisition and analysis were performed with Opus 7 software.

The optical properties of PDA and Melanin NPs were characterized using a UV-vis spectrophotometer (Shimadzu UV-1800, Shimadzu Corporation, Japan) in the wavelength range of 200–800 nm.

2.4.4. Raman spectroscopy. Raman spectra were collected with a μ–Raman LABRAM supplied by Horiba–Jobin–Yvon equipped with a CCD (256 × 1024 pixels) detector cooled at −70 °C and an external laser source: Nd:YAG, λ = 532 nm emission and 50 mW power (Laser output). A 50× Olympus objective was used to explore the surface of the samples and to collect the Raman spectra. The representative Raman shown in the paper have been collected with an acquisition time of 10 s and 25 scans in order to improve the ration signal/noise. The used grating is 1800 g mm^{-1} and the spectral resolution was about 1 cm^{-1}.

The samples, made by powders, were transferred, in micro quantities, on microscope slides and then placed under the objective of the μ-Raman instrument where, after the

acquisition setting parameters, the spectra collections have been performed.

2.4.5. Transmission electronic microscopy (TEM). TEM images (JOEL JEM-1400 Plus electron microscope, JEOL, MI, Italy) were taken at 80 kV. NPs were dispersed in deionized water at concentration 100 μg mL^{-1}. TEM samples were prepared by placing a drop of water solution of both PDA and SM NPs, directly on a copper grid, and left to dry for 24 h.

2.4.6. Thermal measurement. For far-field thermal measurement, a COHERENT Verdi λ = 532 nm CW laser has been used as source. A pinhole with a diameter of 3 mm has been used to reduce the beam spot. The far-field thermal measurement has been acquired using an IR camera FLIR E40 having an IR resolution of 160 × 120 pixel, spatial resolution (IFOV) of 2.72 mrad per pixel and maximum acquired temperature of 650 °C. The measurement started 3 seconds prior the beam impinges on the sample for 5 minutes. Then, the beam is shut-off and the temperature decay is measured for 5 minutes.

During the measurement, the PDA solutions are stirred using a magnetic stirrer.

2.5. Statistical analysis

Each experiment was performed at least three times. Graphically, results were displayed as mean ± standard deviation. The data was subjected to the *t*-test and one-way ANOVA to determine statistical significance. Values of $p < 0.05$ were considered statistically significant.

3. Results and discussion

3.1. Morphology and size analysis of PDA NPs

The reaction of oxidative polymerization proceeded for 24 hours, and the morphological analysis of synthesized PDA NPs after 1 and 24 hours was performed by SEM experiments. The average size of NPs was determined on *ca.* 100 nanoparticles by using ImageJ software. In all samples, the amount of dopamine was kept constant at 50 mg mL^{-1} as well as the H_2O/alcohol volume ratio.

Fig. 1(a–g) presents SEM images of PDA nanoparticles obtained after 1 hour of reaction at increasing NH_4OH concentrations.

SEM analysis demonstrates that the oxidant concentration plays a critical role in determining particle morphology, including size, shape, and distribution uniformity. At lower oxidant concentrations (0.056–0.22%), PDA NPs exhibited irregular shapes, broad size distributions, and frequent aggregation, indicating incomplete or slow polymerization (Fig. 1a–c); from (d) to (e), the particles look more uniform and spherical, with a noticeable improvement in size consistency and a reduction of irregular particles; from (f) to (g), PDA NPs are highly uniform, spherical, and separated. There is a noticeable decrease in particle size, indicating that high NH_4OH concentrations favor the formation of smaller, more monodisperse particles. In Fig. 1(f), particularly, NPs show high monodispersity (uniformity in size), indicating that higher NH_4OH concentrations help the control of both particle growth and aggregation, resulting in more defined particles. This aspect was further evidenced in the plot of the size distribution reported in Fig. 2 showing that [NH_4OH] is a critical factor in controlling particle size and uniformity. At low concentrations (*e.g.*, 0.056%) we obtained larger average particle sizes with a wider distribution, whereas at intermediate concentrations (*e.g.*, 0.89%) we have smaller, more narrowly distributed particles. The distribution was more symmetrical, indicating a better uniformity of particles. At the highest concentration tested (3.58%), the average particle size markedly decreased, accompanied by a significantly narrower size distribution, while at 1.79%, only the distribution narrowed without a substantial reduction in average size, indicative of enhanced control over nucleation and growth. The range of particle size and uniformity was

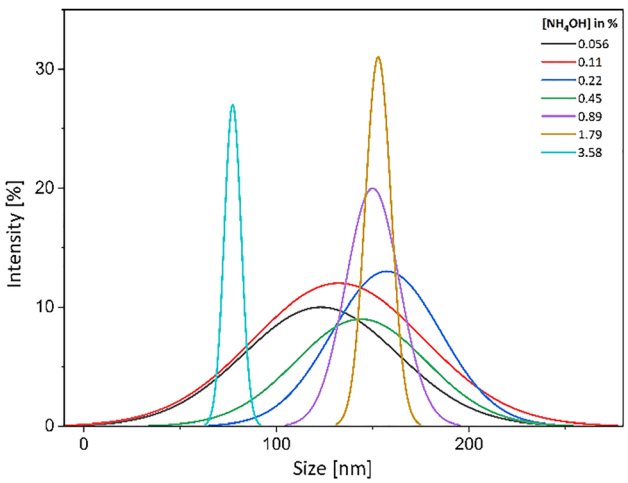

Fig. 2 Morphological parameters of PDA NPs, after 1 h of reaction. The plot shows the particle size distribution as a function of the intensity (%) for various concentrations of [NH_4OH] in percentages. Each curve corresponds to a different concentration of oxidant.

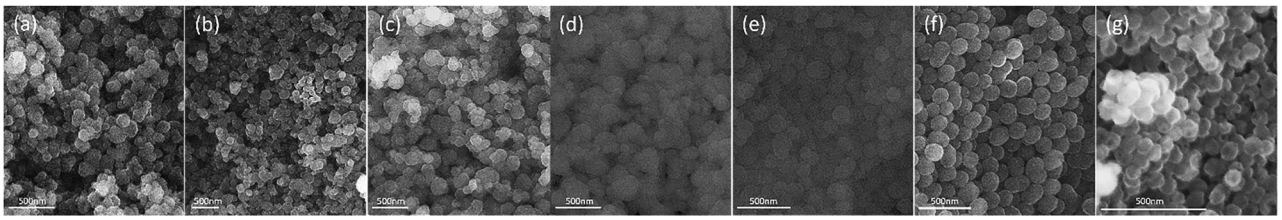

Fig. 1 SEM images of PDA NPs, after 1 h, at different NH_4OH percentages; (a) 0.056%, (b) 0.11%, (c) 0.22%, (d) 0.45%, (e) 0.89%, (f) 1.79% and (g) 3.58%.

Table 1 Statistical properties of PDA nanoparticles synthesized at different NH_4OH concentrations after 1 h (mean ± SD, n = 100). [a,b,c]indicate statistically significant differences ($p < 0.05$) determined by one-way ANOVA followed by t-tests. The values sharing the same letter are not significantly different

[NH_4OH] in %	$\mu \pm \sigma$ (nm)	PdI
0.056	123.05 ± 39.95[a]	0.10
0.11	132.35 ± 44.50[ab]	0.11
0.22	157.24* ± 33.80[b]	0.03
0.45	143.90 ± 28.30[b]	0.05
0.89	149.97 ± 13.88[b]	0.01
1.79	152.84 ± 6.70[b]	0.002
3.58	77.35 ± 4.37[c]	0.003

quantified by the polydispersity index (PdI), a dimensionless measure used to describe how uniform or diverse in size the particles are.

This index can be calculated using eqn (1):

$$\mathrm{PdI} = \left(\frac{\sigma}{\mu}\right)^2 \quad (1)$$

where σ is the standard deviation of the particle size distribution and μ is the mean particle size.

After 1 hour of reaction, the particle size of PDA nanoparticles was significantly influenced by the NH_4OH concentration (ANOVA followed by t-tests, $p < 0.05$). Samples synthesized at concentrations ranging from 0.22% to 1.79% NH_4OH exhibited the largest particle sizes and were statistically indistinguishable (*b*), suggesting similar nucleation and growth dynamics under moderate oxidizing conditions (Table 1).

The sample at 3.58% NH_4OH showed a significantly smaller size and was grouped separately, indicating that high oxidant levels limit particle growth. Intermediate values at 0.056% and 0.11% formed distinct groups, reflecting the balance between slow oxidation and early-stage aggregation.

A comparable trend was observed for the polydispersity index (PdI), reflecting changes in population uniformity as a function of oxidant concentration. At lower oxidant concentrations (0.056–0.11%), the PdI values were relatively high (0.10–0.11), indicating heterogeneous populations and broad size distributions. With increasing NH_4OH concentration, PdI values progressively decreased, reaching extremely low values at 0.89% (0.01), 1.79% (0.002), and 3.58% (0.003). These results suggest that oxidant concentration is a critical parameter for tuning both particle size and uniformity during the early stage of PDA formation, promoting the formation of monodisperse NPs populations, likely due to more efficient and synchronized nucleation during the early stages of PDA formation.

Prolonging the synthesis time for 24 hours reveals the importance of using the optimal concentration of oxidant, which is necessary to initiate dopamine oxidative polymerization. Fig. 3 shows a series of SEM measurements of PDA NPs synthesized with increasing concentrations of NH_4OH from 0.056 to 3.58%, after 24 h of reaction.

Fig. 3 from (a) to (c) confirmed that lower ammonium concentrations (0.056%, 0.11% and 0.22%) lead to incomplete growth or nucleation, resulting in irregular and less dense nanoparticle structures. As the ammonium concentration increased to 0.45% and 0.89%, NPs growth accelerated, producing denser aggregates with reduced interparticle spacing and improved morphological uniformity. The related NPs, shown in Fig. 3d and e, are more uniform in size and shape, and individual boundaries are visible however for 0.89% there was a slight decrease in packing density compared to 0.45%. Fig. 3(f) and (g), referring to 1.79% and 3.58% ammonium concentration, suggests that at this high concentration ammonium plays a role in limiting particle size while maintaining uniformity due to stabilization effects that prevent further aggregation likely driven by enhanced electrostatic repulsion and stabilization of surface charges, which prevented excessive clustering. Lower ammonium concentrations (*e.g.*, 0.056%) show larger size and broader distributions, while higher concentrations of ammonium lead to sharper and more defined peaks, suggesting more uniform particle sizes. The 1.79% NH_4OH sample displayed a narrow, high-intensity peak, indicative of an optimal balance between particle size and colloidal uniformity, as shown in Fig. 4.

The particle size of PDA nanoparticles after 24 hours of oxidation was significantly influenced by the NH_4OH concentration, as confirmed by one-way ANOVA, followed by t-tests (Table 2).

The largest particles were observed at 0.056% and 3.58% NH_4OH (a), while significantly smaller nanoparticles were found in the intermediate concentration range of 0.11% to 1.79% (b). The sample at 0.45% showed intermediate behavior (ab), not significantly different from either group. This trend indicates that moderate NH_4OH concentrations promote the formation of smaller particles, likely due to balanced oxidation and nucleation processes. At low (0.056%) or very high (3.58%) NH_4OH concentrations, larger particles formed, possibly because of insufficient nucleation or uncontrolled growth. PdI values support this interpretation. High PdI values (0.07–0.12) were observed at 0.056–0.450%, indicating broader particle size distributions. In contrast, at higher NH_4OH levels (1.79% and 3.58%), PdI values dropped sharply ($\leq$0.007), suggesting the

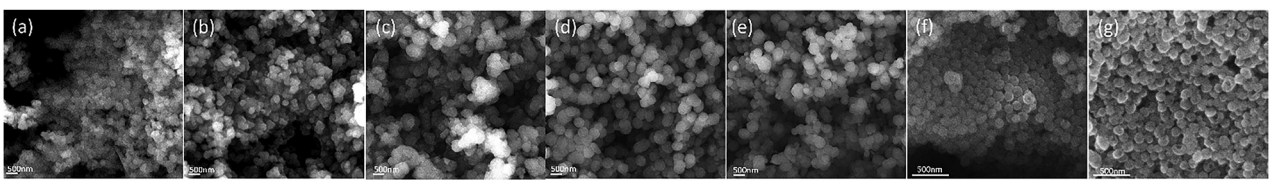

Fig. 3 SEM images of PDA NPs, after 24 h, at different NH_4OH percentage; (a) 0.056%, (b) 0.11%, (c) 0.22%, (d) 0.45%, (e) 0.89%, (f) 1.79%, and (g) 3.58%.

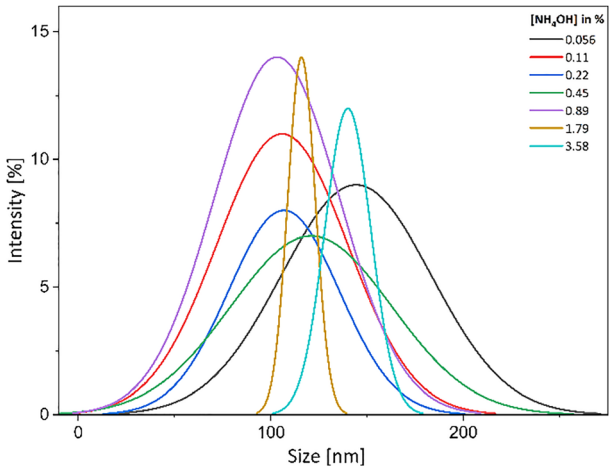

Fig. 4 Morphological parameters of PDA NPs, after 24 h of reaction. (a) the plot shows the particle size distribution as a function of the intensity (%) for various concentrations of [NH_4OH] in percentages. Each curve corresponds to a different concentration of oxidant.

Table 2 Statistical properties of PDA nanoparticles synthesized at different NH_4OH concentrations after 24 h (mean ± SD, n = 100).[a,b]indicate statistically significant differences ($p < 0.05$) determined by one-way ANOVA followed by t-tests. Values sharing the same letter are not significantly different

[NH_4OH] in %	$\mu \pm \sigma$ (nm)	PdI
0.056	144.39 ± 38.98[a]	0.07
0.11	10596 ± 34.01[b]	0.10
0.22	106.81 ± 28.81[b]	0.07
0.45	121.02 ± 41.80[ab]	0.12
0.89	103.19 ± 32.51[b]	0.09
1.79	115.96 ± 7.14[b]	0.003
3.58	140.01 ± 11.93[a]	0.007

formation of more uniform and monodisperse particles under high oxidative strength, where faster polymerization and homogeneous nucleation promote the formation of narrowly distributed NPs.

Prolonging the reaction time has an impact on the particle size, with longer times favouring a continued growth. However, the extent of growth depends on ammonium concentration. In fact, at low ammonium levels, the extended growth determines an increase of particles aggregation, while higher ammonium levels allow for controlled, stable growth limiting the particles aggregation. At low oxidant concentrations (*e.g.*, 0.056%), prolonged reaction times led to extensive aggregation and irregular particle formation, emphasizing the need for sufficient oxidative potential for stable growth. In contrast, using 1.79% NH_4OH for one hour yields uniform, monodisperse nanoparticles, and extending the reaction to 24 hours further enhances their definition and quality. This suggested that this oxidant concentration stabilised growth over time. As growth progressed, longer reaction times typically resulted in larger particles. However, the influence of time on particle growth was mitigated by NH_4OH concentration. There was overlap between different size distribution curves, especially around the 100–150 nm range, where several oxidant concentrations exhibited significant intensities. This suggested that multiple concentrations produced particles of similar sizes within this range. The synthesis process of PDA nanoparticles has been thoroughly studied,[30,33,34] with research highlighting how factors like ammonium concentration and reaction time influence their size, stability, and morphology.[35,36] Furthermore, researchers noted that high hydroxide concentrations (up to 2.5%) promote particle uniformity and inhibit aggregation over time, whereas low concentrations (down to 1%) cause more variation in sizes and promote aggregation, especially at extended reaction times.[37,38] Literature data provided strong support for the influence of ammonium concentration and reaction time on the synthesis of PDA nanoparticles,[35,36,39–41] confirming the relationship between these parameters and the resulting particle size, uniformity, and aggregation behaviour, according with our results.

Comparing the results obtained after 1 h and 24 h of reaction, using increasing concentrations of NH_4OH, we could conclude that the NH_4OH percentage of 1.79% represented the best value, being a good compromise between particle size and uniformity. This concentration (1.79% of NH_4OH) appeared to effectively control the polymerization and growth rate, yielding uniform particles with minimal agglomeration. Based on this result, further experiments designed to characterize PDA NPs were performed on NPs obtained after 24 h using 1.79% NH_4OH, hereinafter referred to simply as PDA NPs.

The features of PDA NPs were compared with the NPs obtained using natural SM isolated from Sepia ink (see Materials and methods). SM was selected as a benchmark material due to its well-documented structural similarity to synthetic PDA NPs. As a non-tunable biopolymer with intrinsic broadband absorption, SM provides a natural reference for assessing the oxidation-dependent adaptability of PDA NPs. This comparison highlights PDA's enhanced tunability, allowing precise control over its properties. Fig. 5 reports the main features of SM particles which have a spherical shape and relatively uniform in size, with an average diameter of 109.21 ± 11.63 nm. A zoomed-in view provided a closer look at the NP morphology; a PdI value close to 0.01 suggests high monodispersity with a very high uniformity in size.

3.2. Effect of NH_4OH concentration and oxidation time

The structural evolution of PDA NPs was evident over time, revealing changes in size, shape, surface texture, and aggregation behaviour. Fig. 6 provides a comparative morphological analysis of PDA NPs, at 1.79% of NH_4OH, formed under long polymerization times, ranging from 48 hours (a) to 120 hours (c).

At 48 hours (Fig. 6a), the NPs exhibited a spherical morphology with smooth, well-defined contours, indicating a stable and relatively uniform structure. The particles were consistent in size, suggesting well-controlled nucleation and early-stage polymerization with minimal aggregation.

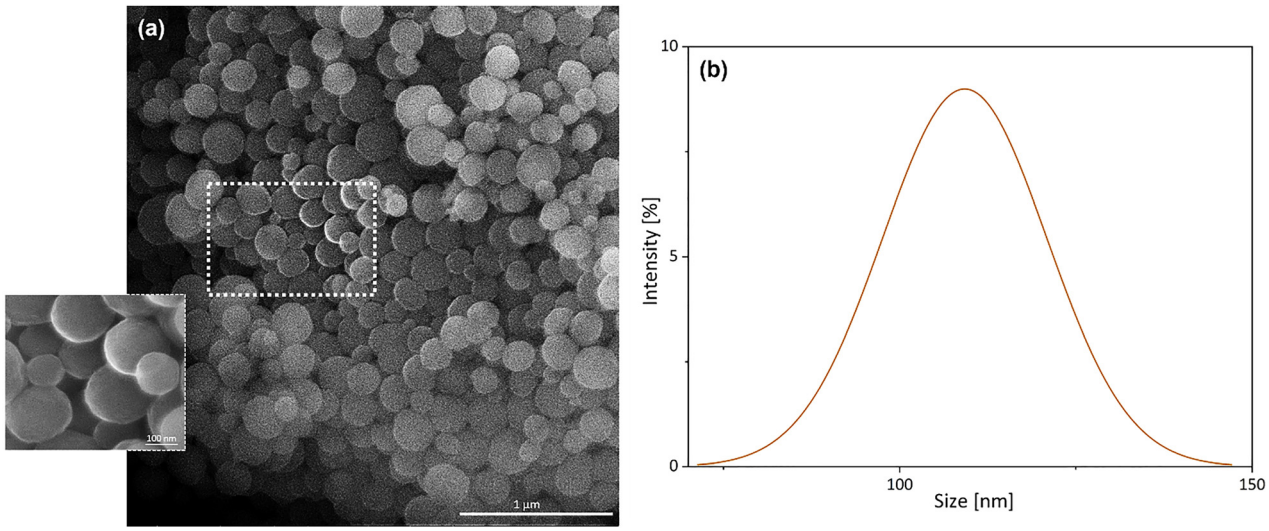

Fig. 5 Nanoparticles obtained using natural melanin extracted from Sepia officinalis. (a) SEM micrographs with an enlargement section; (b) size distribution of SM NPs.

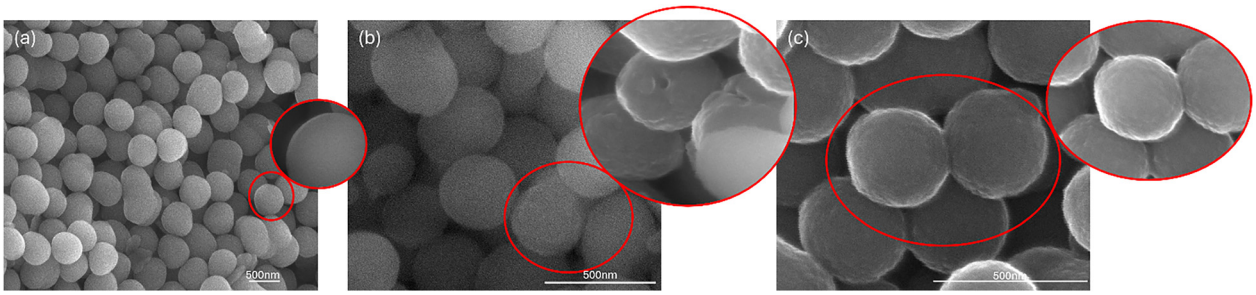

Fig. 6 SEM images of PDA NPs synthesized at 1.79% NH_4OH percentage, captured at different reaction times: (a) 48, (b) 96, and (c) 120 hours. The data demonstrates a significant evolution in nanoparticle morphology and aggregation as the reaction time increased.

Between 48 and 96 hours, particle size variation increased, with larger clusters and aggregates forming, suggesting coalescence and particle fusion. Surface roughness also became more pronounced, likely due to continuous polymer deposition.[42] By 96 hours (Fig. 6b), layering and aggregation intensified, and network-like structures began to emerge. This stage marked a shift toward partial–particle fusion, leading to increased roughness and irregular surface textures.

Surface roughness evolution was also observed. In the early stage (1–24 h), the NPs were primarily solid and uniform, exhibiting minimal surface roughness (see Fig. 1 and 3). From 48 h to 96 h, a gradual increase in surface modifications became evident, with visible surface roughness and microstructural changes in individual nanoparticles. At 120 hours (Fig. 6c), highly superficial areas and interconnected structures were observed, indicating an advanced polymerization and aggregation state.

Moreover, as the reaction progressed, slight elongation and reduced symmetry were also noted, likely due to continuous growth, aggregation, and molecular rearrangements. The surface morphology of PDA NPs remained highly sensitive to reaction time, with extended polymerization influencing roughness, and functional group density.[27] As dopamine oxidation continued, new polymer layers formed, leading to a rougher texture and increased interparticle adhesion, possibly due to enhanced hydrophobic interactions and π–π stacking.

At 120 hours, the PDA NPs reached their highest degree of roughness, with a distinct network-like morphology, likely resulting from secondary nucleation and coalescence. This phenomenon may involve smaller particles merging with larger ones, contributing to the observed aggregated structure.[43]

These morphological transformations aligned with the expected growth mechanism of PDA NPs. In fact, in the early stages (48 h), smooth and spherical particles formed due to dominant nucleation. At 96 hours, progressive polymerization induced surface texturing and layered deposition. Finally, after 120 hours, continued dopamine oxidation and polymer cross-linking led to the formation of larger and rougher, emphasizing the role of oxidative polymerization in shaping PDA NP morphology.

3.3. Hydrodynamic diameter and colloidal stability

Once the synthesis conditions were optimized at 1.79% NH_4OH, the colloidal properties of PDA NPs, including

Table 3 Hydrodynamic diameter (D_H), polydispersity index (PdI), and zeta potential (ζ) of PDA NPs synthesis over a period of 120 h

Sample	Size (D_H; nm)	PdI	Zeta potential (ζ; mV)
1 h	194.6 ± 4.1	0.063 ± 0.036	−38.0 ± 2.87
24 h	154.1 ± 8.6	0.049 ± 0.029	−41 ± 2.8
48 h	221.1 ± 3.6	0.099 ± 0.043	−29.1 ± 2.6
96 h	216.7 ± 2.6	0.102 ± 0.038	−25.3 ± 1.9
120 h	226.6 ± 1.2	0.115 ± 0.024	−20.5 ± 5.0

hydrodynamic diameter (D_H), polydispersity index (PdI), and zeta potential (ζ) were systematically analyzed over a 120-h reaction period. As observed in Table 3, in the early phase (1 h to 24 h), a decrease in D_H was observed, alongside a slight reduction in PdI and a shift in ζ toward more negative values.

This suggests a stabilization period during which particle nucleation and structural compaction occur, supported by SEM images showing well-dispersed spherical particles. The increased negative ζ indicates stronger electrostatic repulsion, helping maintain colloidal stability. After 24 hours, a reverse trend emerged. Both D_H and PdI progressively increased, while the ζ potential became less negative. By 48 hours, the increase in D_H and PdI, along with the reduced ζ, pointed to the onset of particle–particle interactions and early aggregation. This trend intensified at 96 h and 120 h, with further increases in D_H and PdI. The reduction in ζ to less negative values (from −41 mV at 24 h to −20.5 mV at 120 h), likely reflects surface restructuring. The increasing D_H and PdI, coupled with a less negative ζ, highlight that for prolonged reaction time the system moves toward colloidal instability, likely due to weakened electrostatic repulsion facilitating NP clustering. A moderate positive correlation was observed between synthesis time and particle size (r = 0.67), although this trend was not statistically significant (p = 0.216). Linear regression analysis yielded a slope of 0.40 nm h^{-1}, indicating a slight increase in D_H over time. These results suggest a general trend of nanoparticle growth during prolonged reaction times, though the variability in the early stages (notably at 24 and 48 h) reduces the robustness of this trend.

3.4. Model-based interpretation of PDA NPs growth

To contextualize the particle size evolution observed in this study, we evaluated the applicability of the empirical model proposed by Alonso *et al.*,[33] which relates the mean particle diameter (D) to dopamine concentration [DA], ammonium hydroxide concentration [NH_4OH], and oxidation time (t) through the eqn (2):

$$D = k\,([NH_4OH]/[DA])^{\alpha}\cdot t^{\beta} \quad (2)$$

where k, α, and β are empirical constants dependent on experimental conditions.

Given that the [DA] was held constant in our synthesis (50 mg mL^{-1}), we focused on the correlation between particle size, oxidant concentration, and reaction time.

For the 1 h dataset (varying [NH_4OH]), we observed a good fit to a power-law dependence, consistent with a nucleation-dominated regime. The inverse relationship between D and [NH_4OH] (with $\alpha > 0$) aligns with the findings of Alonso *et al.*[33] and others investigating early-stage PDA polymerization kinetics.[44,45]

In contrast, data collected at 24 h began to deviate from the model. This can be attributed to the competing kinetics of nucleation and secondary growth/aggregation, which are not explicitly captured in Alonso's simplified model.

For the extended oxidation times (48–120 h) at fixed [NH_4OH], the empirical model fails to predict the observed non-monotonic size evolution, characterized by initial compaction followed by subsequent growth and aggregation. These deviations likely arise from complex phenomena, including structural densification, oxidative crosslinking, and evolving surface charges—parameters not explicitly included in the original empirical formulation. Similar limitations have been reported in related studies, where single-single models were insufficient to describe the multistage growth of PDA NPs under varying redox conditions or without thermal activation.[46,47]

At early oxidation stages (1 h), our results demonstrated a clear inverse dependence of particle diameter on [NH_4OH] with log–log regression suggesting good agreement with the predicted power-law behavior. This supports a nucleation-dominated mechanism consistent with Alonso's model. However, for longer reaction times, particularly beyond 48 h, additional physicochemical factors dominate and deviations from the model become evident. These discrepancies arise from structural transformations—including polymer densification, crosslinking, aggregation, and surface roughness evolution—which are not explicitly accounted for in the original empirical formulation.[33,34] Therefore, while the Alonso model provides a valuable framework for interpreting the early-stage dynamics of PDA formation under controlled conditions, its predictive capacity diminishes in more complex, time-evolving systems. Furthermore, the prediction of experimental results loses effectiveness if the reaction is conducted without heating. Similar observations were reported in later-stage PDA growth studies, which suggest that single-regime scaling laws lose predictive accuracy beyond initial nucleation.[30] These findings underscore the importance of considering multistage growth and molecular reorganization phenomena in the long-term oxidation of PDA NPs. Therefore, a constant dopamine concentration over prolonged reaction times could explain the observed non-monotonic particle size variations, where oxidative fragmentation and structural rearrangement mechanisms become progressively significant, ultimately governing particle dimensions and morphological characteristics. To further illustrate the limitations of the Alonso at al.[33] model over extended oxidation periods, we applied the empirical fitting to the particle size data collected at increasing oxidation times, under fixed [NH_4OH] and [DA]. As shown in Fig. S1, the resulting fit yields an R^2 value of 0.45, indicating only a moderate correlation. This supports the conclusion that the model's predictive

accuracy diminishes beyond the nucleation-dominated regime, where complex structural reorganizations such as aggregation and oxidative crosslinking become dominant.

3.5. TEM analysis

Fig. 7 shows TEM images of PDA (a) and SM (b) NPs, as reference. As can be seen, TEM images corroborate the data obtained from SEM morphological analysis. Both PDA (a) and SM (b) NPs showed a roughly circular, well-defined shape, indicating that both samples likely consisted of similar-sized spherical particles. The uniformity of the edges suggested good particle morphology and potentially uniform synthesis conditions in the case of PDA NPs (Fig. 7a). It can be observed as the image contrast varied as a consequence of polymerization time. SM NPs in Fig. 7b appeared to have higher contrast than PDA NPs in (a).

The alterations in TEM contrast are attributable to fluctuations in electron densities on the image plane. They are conceivable to be associated with NPs consolidation over time, consequently resulting in elevated degrees of polymerization and densification. In TEM analysis, the contrast differences could indicate a variation in particle thickness or density. A denser or thicker particle would appear darker due to increased electron scattering, suggesting that the SM particle in (b) might be either thicker or denser than PDA NPs in (a).

The edges of PDA NPs in Fig. 6a appeared slightly less defined, or ''fuzzier'', compared to the sharp edge of SM in 7 b. TEM contrast changes represented the consequence of electron densities variations, that could be related to PDA NPs (a) polymerization and densification degree with respect to SM NPs (b). This could indicate different surface properties, such as roughness, of the nanoparticle in (a) that scattered electrons more diffusely, compared to SM particle in (b). The lack of internal structural details in both images could imply that these particles are either amorphous or too small for internal features to be resolved at this operating voltage.

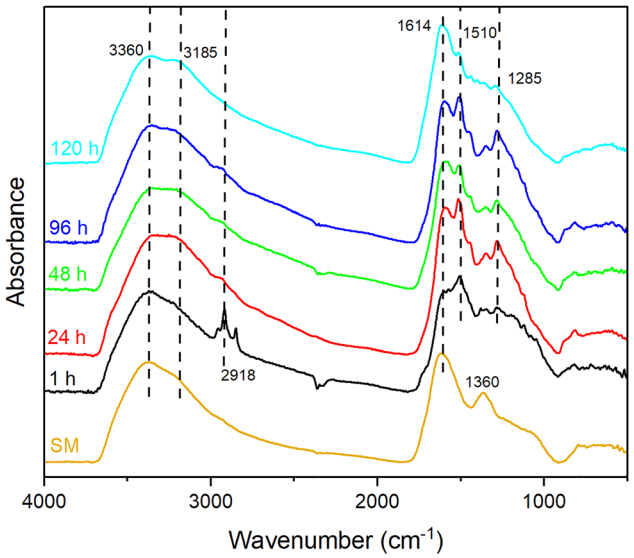

Fig. 8 FTIR absorption spectra of PDA NPs at 1.79% of NH_4OH percentage at different reaction time. For comparison, the absorbance spectrum of SM is also shown on the bottom.

3.5. FTIR characterization of PDA NPs

The molecular structure of the NPA NPs was characterized by the Fourier transform infrared (FTIR) spectroscopy. Fig. 8 shows the FTIR absorption spectra of PDA NPs at 1.79% of NH_4OH percentage as a function of reaction times. The absorbance spectrum of SM used here as a reference compound is also shown.

The samples show characteristic vibrational peaks consistent with literature data[19,29,30] with a broad band between 3600–3000 cm^{-1} where overlap the stretching vibration of the N–H and O–H bonds of amine, amide, carboxylic acid, phenolic, and aromatic amino functional groups. The peaks between 1750 and 1500 cm^{-1} are usually assigned to C═C and C═O stretching vibration of aromatic compounds.[48]

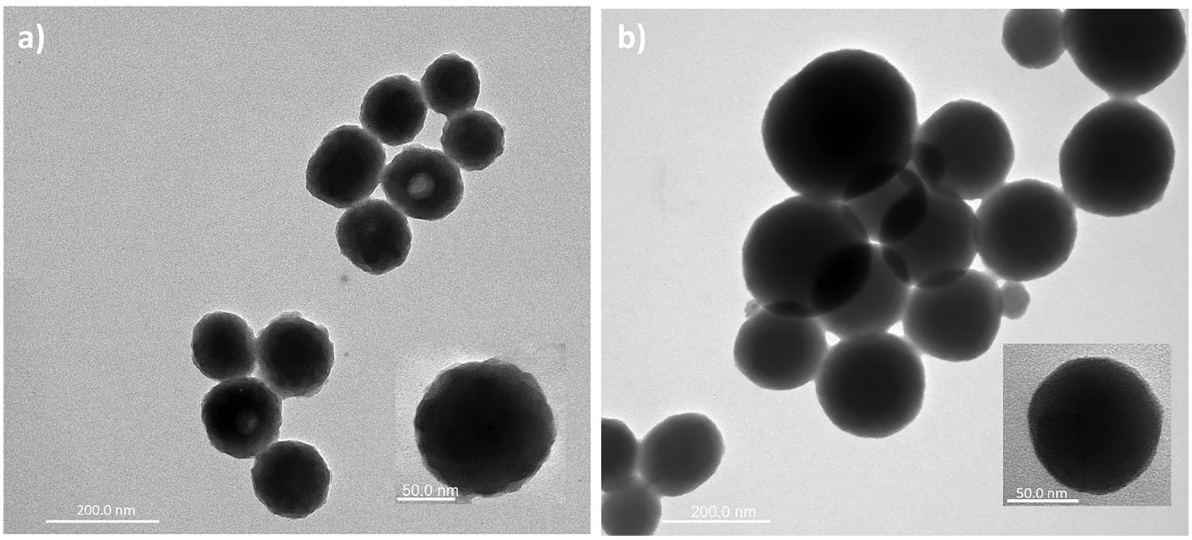

Fig. 7 TEM image of PDA NPs (a) and SM, NPs obtained with natural melanin extracted from *Sepia officinalis* (b).

Specifically, the reference FTIR spectrum of SM showed prominent peaks at 3385 cm^{-1}, 1620 cm^{-1}, and 1360 cm^{-1}, corresponding to O–H/N–H, C═C, and C–OH groups, respectively.[49]

The spectra of PDA NPs show similar peak patterns to SM NPs with variations in peak intensities, suggesting possible changes in the functional group interactions or overall concentration. In particular, the band at 3360 cm^{-1} show a shoulder at 3185 cm^{-1} which increases with the reaction time, suggesting accumulation of phenolic groups. The peaks at 2918 cm^{-1} are assigned to the C–H stretching vibrations in aliphatic (non-aromatic) hydrocarbons. The presence of such peaks at the early stage of the oxidation suggests an incomplete aromatization or polymerization. As the reaction progresses to 24 h, these peaks disappear reflecting the gradual transformation of aliphatic into aromatic structures that are characteristic of mature, crosslinked PDA.

The peaks in the 1500–1600 cm^{-1} region are characteristic of carbon–carbon skeletal stretching vibration in the aromatic ring. The bands at 1614 and 1510 cm^{-1} became more resolved with the reaction time suggesting more pronounced aromatic structures or a higher degree of conjugation.

Enhancement of polymerization degree, leading to a more mature PDA structure with an increased number of aromatic and crosslinked bonds, was reached also extending the reaction time. The peak at 1285 cm^{-1} corresponds to the stretching vibration of catechol hydroxyl C–O and/or C–N. The intensity of this peak increass after 24 h possibly due to crosslinking and aromatic ring formation that establish a more complex, π-conjugated structure that gave PDA its characteristic dark color.

In the late stages, from 96 to 120 h, the structure had transformed into a highly crosslinked and aromatic network. This stage represented a stabilized structure with rich surface functionalities and a highly crosslinked aromatic core. The peak increase at 1614 cm^{-1}, and the stabilization of the complementary peak at 1285 cm^{-1}, indicates an oxidative conversion of catechol/phenol groups into quinone structures, characteristic of advanced PDA polymerization and aging.

3.6. Raman spectroscopy characterization

Fig. 9 reports representative Raman spectra collected on the PDA NPs samples at different oxidation reaction times: 1 h, 24 h, 48 h, 96 h, and 120 h.

As it can be seen, the main Raman features are detectable in the range between 975 and 1820 cm^{-1}. In particular, the two bands at about 1365 and 1580 cm^{-1} represent the bands D and G of the graphite systems, respectively. The wide band at about 2750 cm^{-1} can be assigned to the presence of the 2D band as in the graphene systems.[50,51] The D band is ascribed to the breathing mode A_{1g} of carbon sp^3 while the G band is assigned to the presence of in plane bond-stretching of all pairs of carbon sp^2.[52,53]

The presence of the D and G bands are typical of the spectra collected on PDA as deposited layer[50,54,55] and represent a partial graphitization of the PDA films.

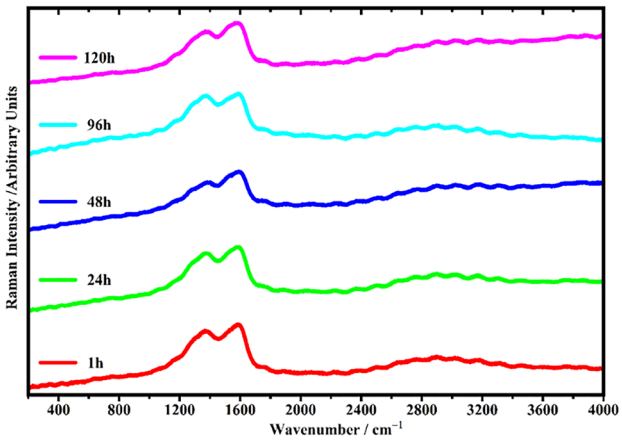

Fig. 9 Representative Raman spectra collected on the PDA samples as a function of the reaction time: 1 h, 24 h, 48 h, 96 h, and 120 h.

In order to study how the oxidation time affects the graphitization of the PDA films, the representative spectra, in the range between 975 cm^{-1} and 1820 cm^{-1}, have been fitted by Gaussian functions.

Fig. 10 are given the fit of the Raman spectra collected on the films at different reaction times.

The D and G bands have been fitted by seven Gaussian functions, and the wavenumber of the peak position is reported in Table 4, as a function of the oxidation time for the different PDA films.

The wavenumbers associated with peak 1 fall in the range between 1054–1063 cm^{-1} (Table 4). These bands are assigned to the C–H stretching modes of the aromatic ring.[56] Similarly, the frequencies associated to the peak 2 fall in the range 1170–1179 cm^{-1} and are assigned to the C–C, C–OH, C–H, and N–H bonds present in amide, phenolic and pyrrole groups.[50] Peak 3 falls in the range 1267–1271 cm^{-1} and can be assigned to the C–O stretching[57]. Peak 4 is in the range between 1373–1384 cm^{-1}. Such bands are ascribed to the C–N–C stretching of the indole aromatic ring.[58] The frequencies of peak 5 fall in the range between 1512–1519 cm^{-1} and have been attributed to the aromatic ring breathing mode with the largest contribution coming from C–N bond.[56] The frequencies associated with peak 6 fall in the range 1599–1604 cm^{-1} and such peak is ascribed to the H–N–C in plane bending vibration.[59] Finally, peak 7 characterized by frequencies in the range between 1733–1745 cm^{-1} can be due to the C═O and C═C stretching modes contributions of aromatic structures of PDA.[50,60,61]

Fig. 11 reports the trends of the I_D/I_G ratio as a function of the oxidation reaction time. The difference between the three graphs shown concerns the way how the intensity of the D and G bands has been calculated.

In the red graph, the intensity of the D band is given by the sum of the intensities of peak 3 and peak 4 and the intensity of the G band is made by the sum of the intensities of peak 5 and peak 6.

In the blue graph, the intensity of the D band is obtained by the sum of the intensities of peak 1, peak 2, peak 3 and peak 4

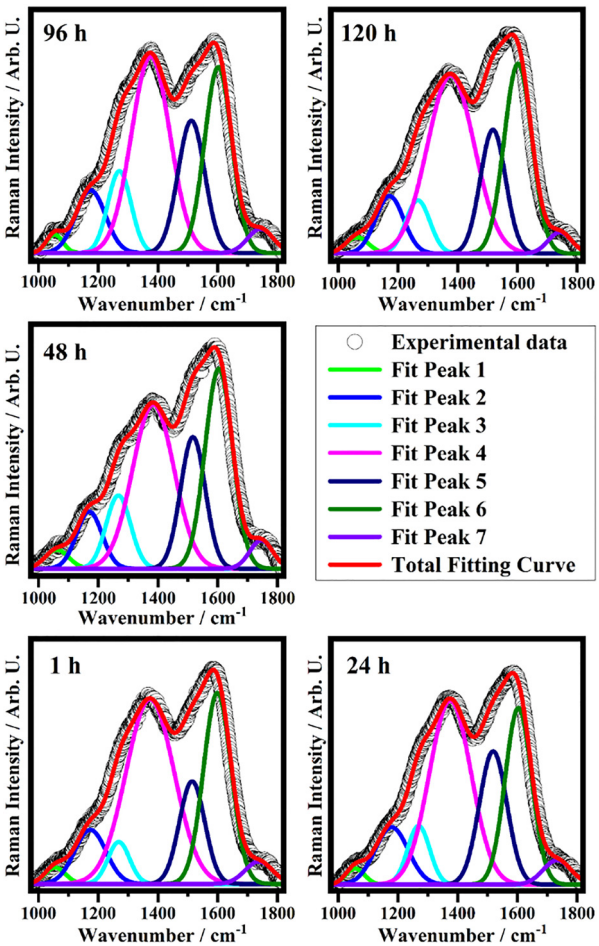

Fig. 10 Fitting of the representative Raman spectra in the range between 975 and 1820 cm^{-1} collected on the PDA NPs samples as a function of the oxidation reaction time: 1 h, 24 h, 48 h, 96 h and 120 h. The open circles are the experimental data, the green, blue, cyan, magenta, navy, olive and violet curves represent the single Gaussian components, and the red curve is the total fitting function obtained during the fitting procedure.

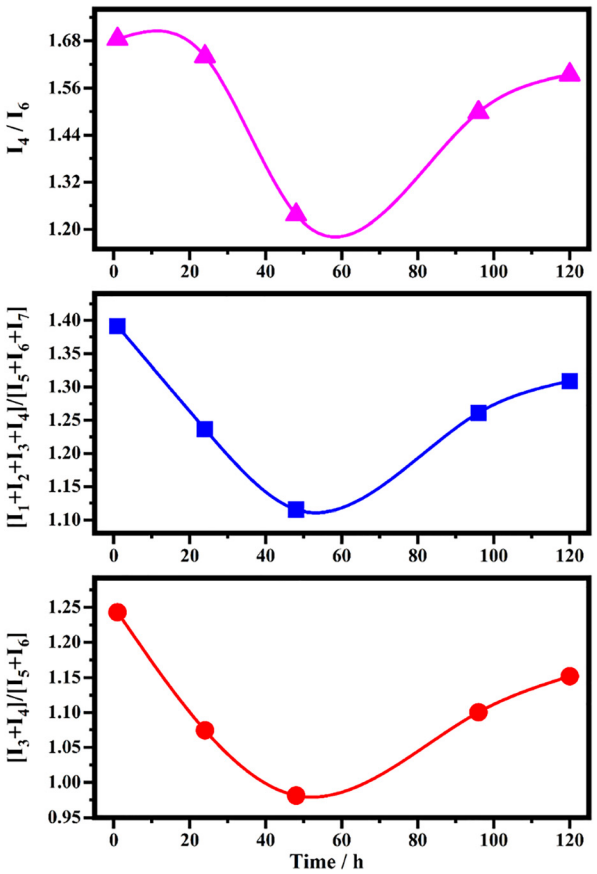

Fig. 11 Intensity ratio (I_D/I_G) between the D and G bands as a function of oxidation reaction time. Different symbols have been used to highlight that the values used to calculate the intensities of the D and G bands differ in the three graphs. Lines joining the symbols are guides to the eye. In the graph on the bottom (red) the intensity of the D band has been obtained by the sum of the intensities of the Gaussian function 3 and Gaussian function 4 while the intensity of the G band has been obtained by the sum of the intensities of the Gaussian function 5 and Gaussian function 6. In the graph on the middle (blue) the intensity of the D band has been obtained by the sum of the intensities of the Gaussian function 1, Gaussian function 2, Gaussian function 3 and Gaussian function 4 while the intensity of the G band has been obtained by the sum of the intensities of the Gaussian function 5, Gaussian function 6 and Gaussian function 7. In the graph on the top (magenta), the intensity of the D band has been considered just the intensity of the Gaussian function 4 while for the intensity of the G band has been used the intensity of the Gaussian function 6. The I_D/I_G ratio decreases from nanocrystalline to amorphous and back to nanocrystalline structure.

and the intensity of the G band is calculated by the sum of the intensities of peak 5, peak 6 and peak 7.

Latter, in the magenta graph, the intensity of the D band is equals of the intensity of peak 4 and the intensity of the G band is equals to the intensity of peak 6.

Even though, quantitative determination of such quantities is beyond the scope of the present work, since the ratio I_4/I_6 span in a greater range with respect to the other intensities ratios ($[I_1 + I_2 + I_3 + I_4]/[I_5 + I_6 + I_7]$, $[I_3 + I_4]/[I_5 + I_6]$), then its

Table 4 Wavenumber of the peak of the Gaussian components used to fit the D and G bands of the spectra collected on the PDA films obtained at different oxidation time

	Wavenumber (cm^{-1})						
Sample	Peak 1 (cm^{-1})	Peak 2 (cm^{-1})	Peak 3 (cm^{-1})	Peak 4 (cm^{-1})	Peak 5 (cm^{-1})	Peak 6 (cm^{-1})	Peak 7 (cm^{-1})
PDA (1 h)	1056	1173	1269	1373	1514	1599	1738
PDA (24 h)	1057	1179	1269	1375	1519	1603	1733
PDA (48 h)	1062	1170	1267	1384	1517	1604	1745
PDA (96 h)	1054	1174	1271	1376	1512	1601	1743
PDA (120 h)	1063	1172	1267	1377	1518	1602	1742

monitoring should allow to better detect the structural changes, eventually occurred, to the analyzed samples.

Anyway, all the three trends shown in Fig. 11, confirm that as well as the oxidation time increases the I_D/I_G ratio decreases and reaches a minimum value around the half of the oxidation time and suddenly it increases to the initial values when the oxidation time goes to 120 h. Such ratio represents the degree of graphitization.[62] Therefore, the graphitization of our samples decreases, in analogy with the I_D/I_G ratio, as well as the oxidation time increases becoming smaller until reaching a minimum value at about 60 hours of oxidation time. Afterwards, the graphitization of the sample increases again reaching approximately the initial values after 120 hours of oxidation time. In other words, the sample starting nano-crystalline but as well as the oxidation time increases it becomes amorphous after 60 hours of oxidation time and, then, further the increase of the oxidation time to 120 h makes the films nano-crystalline again.[54] This result indicates that the PDA NPs, as a function of the oxidation time, goes through three different phases: the first nano-crystalline, the second amorphous and the third nano-crystalline again, maybe, different from the first one.

3.7. Optical properties and Thermal measurements of PDA NPs

The absorbance spectrum of PDA NPs, recorded in water at a concentration of 100 μg mL^{-1} and showed in Fig. 12a, exhibited a broad absorption profile spanning the ultraviolet to visible range. This is consistent with the typical characteristics of the PDA structure, which showed a wide absorption band due to its conjugated polymeric structure, allowing for various electronic transitions. The highest absorbance was observed in the UV range (200–300 nm), with a gradual decrease as the wavelength increased. This high UV absorbance was characteristic of the π–π* transitions within the aromatic rings of PDA. The absence of distinct peaks in the visible range indicates that PDA NPs did not exhibit selective absorbance at these wavelengths. This aligned with their general broadband absorption characteristic rather than selective chromophoric behaviour.[49,63] In Fig. 12a, we reported the spectrum of SM NPs, as a reference, characterized by a broad absorption that extends from the UV to the visible range (200–800 nm), typical for melanins,[49,64] which had complex, heterogeneous structures that enabled various types of electronic transitions. This feature is consistent with melanin's role as a natural pigment with photo-protective properties against UV radiation. The broadband absorption observed in the UV-vis spectra of the PDA NPs, a characteristic feature of melanin-like materials, is directly correlated with their ability to efficiently convert absorbed light into heat through non-radiative relaxation processes, thereby justifying the subsequent thermal measurements.

The photothermal response of PDA nanoparticles varied significantly with oxidation time. Statistical analysis (one-way ANOVA followed by *t*-tests, $p < 0.05$) revealed that PDA NPs at 1 h, 96 h, and 120 h exhibited significantly higher ΔT values than Sepiamelanin NPs (a), while 24 h and 48 h samples showed comparable values (b).

The PDA NPs performance was evaluated under different oxidation times, revealing a nonlinear trend in temperature response. The temperature variation (ΔT) varied significantly with oxidation conditions, with an initial decrease from 1 h to 48 h, followed by a recovery at 96 h and 120 h (Fig. 12b). This behaviour is strongly influenced by oxidation-induced structural changes, primarily crosslinking density, and surface roughness, which evolve. These modifications directly affect electron delocalization, light absorption efficiency, and thermal diffusion, ultimately governing light-to-heat conversion efficiency. This behaviour correlates strongly with structural modifications observed in SEM, FTIR, and Raman analysis, where crosslinking and surface roughness emerge as the dominant factors influencing photothermal efficiency. FTIR analysis (Fig. 8)

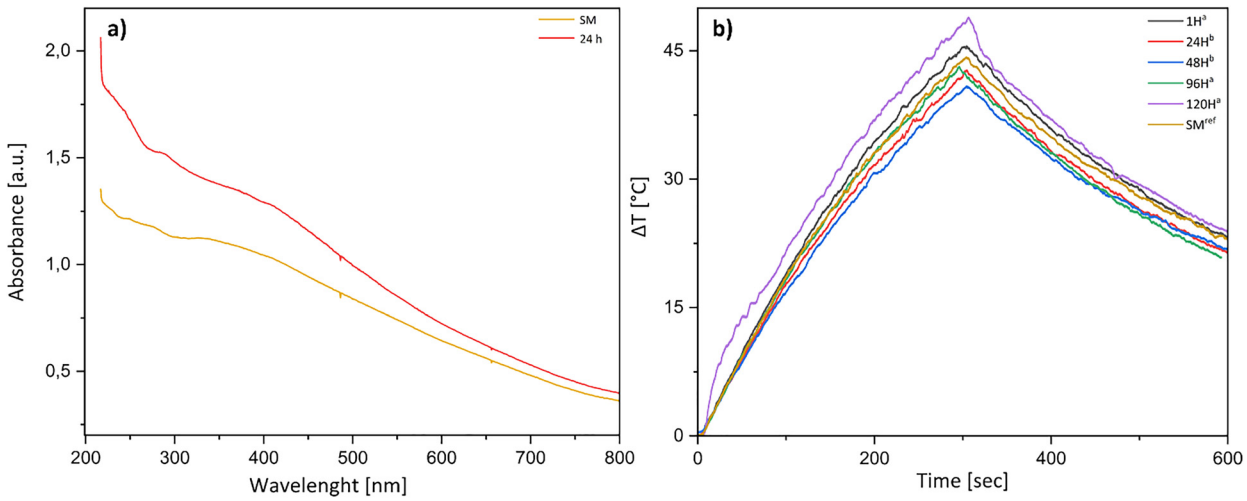

Fig. 12 (a) Absorption spectrum of PDA NPs after 24 h (red line) and of SM extracted from *Sepia officinalis* (yellow line), used as reference; (b) Temperature variation (ΔT) as a function of illuminating time (seconds) for PDA NPs at different oxidation stages: 1 (black line), 24 (red), 48 (blue), 96 (green), and 120 hours (purple). The photothermal conversion capability of SM is shown for comparison (yellow line).

confirms a progressive oxidation of catechol (–OH) groups into quinones, leading to increased intramolecular crosslinking and polymeric rigidity. This oxidation process results in structural densification, reducing free charge carriers, as further evidenced by Raman spectroscopy, which reveals enhanced π–π stacking interactions. These effects restrict electron delocalization, which is essential for efficient photothermal conversion *via* non-radiative relaxation mechanisms. At short oxidation times (1 h and 24 h; black and red lines in Fig. 12b, respectively), the high availability of catechol and amine groups promotes strong electron delocalization. This mechanism underlies the elevated ΔT values observed at these time points (47.9 ± 0.1 °C and 45.0 ± 0.1 °C, respectively). However, at 48 h (blue line), crosslinking reaches a critical threshold, severely limiting charge mobility, leading to the lowest ΔT (44.0 °C ± 0.1). This observation confirms that excessive oxidation disrupts photothermal efficiency by reducing the density of free charge carriers capable of participating in photo-induced energy transfer mechanisms. While crosslinking is the primary limiting factor, SEM analysis reveals that prolonged oxidation (Fig. 6), induces significant surface roughness. This fact enhances light scattering and absorption, which partially compensates for the loss of charge mobility due to crosslinking. The recovery in ΔT at 96 h (47.9 °C ± 0.1) and 120 h (48.9 °C ± 0.1) is attributed to these surface modifications, which increase photon capture efficiency. This trade-off between light absorption enhancement and thermal diffusion acceleration suggests that surface modification alone cannot fully restore photothermal efficiency once electron mobility has been significantly restricted. Thus, crosslinking remains the dominant determinant of photothermal performance, while surface morphology modification acts as a secondary modulating factor. However, increased roughness also accelerates thermal diffusion, leading to faster heat dissipation and potentially reducing heat retention time. Zhang *et al.* (2021) reported that highly rough PDA nanostructures exhibit increased thermal diffusion, which can reduce the efficiency of local heat retention, particularly in hyperthermia applications.[36] A similar trend was reported by Liu *et al.*, where PDA nanospheres exhibited optimal photothermal efficiency at shorter reaction times, whereas prolonged polymerization led to reduced absorption efficiency due to increased molecular rigidity and oxidation-driven densification;[19] additionally, Chen *et al.* (2016), observed that increasing PDA crosslinking density reduced charge transfer efficiency, leading to lower heat conversion efficiency in highly oxidized PDA films.[42] As a comparative reference, SM (yellow line in Fig. 12b), was used as a benchmark for synthetic PDA materials. Studies have shown that SM NPs exhibit efficient light-to-heat conversion under near-infrared (NIR) excitation, making them promising candidates for photothermal therapy.[65] However, its photothermal performance is inherently lower than PDA nanoparticles, as observed in the thermal profile of SM (ΔT 44.2 °C ± 0.1), which remains below the values observed for PDA NPs at 1 h and 120 h (black and purple lines in Fig. 12b). The lower photothermal efficiency of SM can be attributed to its rigid, pre-formed molecular structure, which lacks oxidation-induced tunability. While PDA undergoes oxidation-dependent crosslinking and roughness evolution, allowing for adjustable photothermal properties, SM remains structurally static, limiting its optimization potential. Additionally, Raman spectroscopy indicates that PDA NPs experience oxidation-dependent π–π stacking changes, whereas SM maintains a stable graphitic-like structure, further restricting its tunability.[65,66] Overall, the photothermal efficiency reduction at 48 h in PDA NPs is primarily due to excessive crosslinking, which restricts electron mobility, whereas the recovery at 96 h and 120 h is linked to increased rougness and superficial areas, which improves light absorption but accelerates cooling. This was in line with studies on PDA-derived carbon materials, where enhanced graphitization at longer oxidation times results in greater electron localization and reduced photothermal conversion efficiency.[67] While SM remains a valuable reference material in photothermal applications, PDA's ability to fine-tune crosslinking and surface features *via* oxidation gives it a strategic advantage in applications requiring adjustable photothermal responses. The photothermal behaviour of the synthesised PDA NPs exhibited a notable temperature elevation ($\Delta T \approx$ 48.9 °C) and this places them among the most efficient organic photothermal nanomaterials reported to date. This performance is comparable to that of well-established inorganic nanostructures, such as gold nanorods[68,69] and carbon-based nanomaterials,[21,70] which typically achieve temperature increases of 45–60 °C under near-infrared (NIR) laser irradiation at similar concentrations and exposure times. Gold NPs display sharp plasmonic absorption and high photothermal conversion under NIR excitation, while carbon nanostructures benefit from strong π–π interactions and thermal conductivity. However, PDA NPs offer the unique advantages of broadband absorption, oxidation-tunable performance and inherent biocompatibility.[19,20,36] Furthermore, in contrast to rigid inorganic systems, PDA enables molecular-level customisation *via* modulation of the oxidation state and crosslinking density,[71] which directly influences electron delocalisation and structural morphology—two critical factors that govern photothermal efficiency. Combined with their aqueous dispersibility and biodegradability, these features suggest that PDA NPs may be a competitive, safer alternative to metallic nanomaterials for photothermal therapy[36,72] and related applications.[44] Future work will involve systematically benchmarking PDA NPs against metallic or carbon-based nanomaterials under standardised optical and thermal conditions to quantify their relative performance more precisely.

4. Conclusions

This study establishes a direct correlation between oxidation-driven structural modifications and photothermal efficiency in PDA NPs. Controlled oxidation leads to progressive catechol-to-quinone conversion, enhancing π–π stacking and intermolecular crosslinking, as confirmed by FTIR and Raman spectroscopy. SEM analysis reveals a transition from dense spherical

NPs to increasingly rough structures, influencing light absorption and thermal behaviour. Photothermal analysis revealed a nonlinear temperature response with respect to oxidation time. Optimal performance was observed at 1 h and 120 h, whereas a decline occurred at 48 h, attributed to excessive crosslinking. Compared to SM ($\Delta T = 44.2 \pm 0.1$ °C), PDA NPs demonstrated greater tunability and responsiveness, enabling more precise control of thermal output through oxidation-state modulation. In addition to structural and thermal characterization, colloidal analysis *via* DLS identified the 24 h sample ($D_H \approx 154$ nm; $\zeta \approx -41$ mV) as the optimal balance point, offering high dispersion stability and uniform particle size—critical parameters for applications in drug delivery and environmental remediation.

These findings highlight PDA's potential for photothermal therapy, drug delivery, and solar energy applications. Future work should explore metallic hybridization (PDA-Ag), *in vivo* stability, and functionalized coatings to broaden applicability. By linking molecular evolution to functional efficiency, this study offers a design framework for next-generation PDA-based nanoplatforms in biomedical and energy-related technologies.

Author contributions

O. G. conceived the idea, designed the experiments, and prepared the manuscript. G. D. performed SEM analysis. G. D. P. conducted DLS analysis and contributed to the writing of the manuscript. R. G. performed FTIR analysis and contributed to the writing of the manuscript. A. N. and M. C. performed Raman spectroscopy experiments and contributed to the writing of the manuscript. A. F. carried out photothermal conversion experiments and contributed to the writing of the manuscript. All authors reviewed and approved the final version of the manuscript.

Conflicts of interest

The authors declare that they have no conflicts of interest that could have appeared to influence the work reported in this paper.

Data availability

All the references/data used for this research are mentioned on the reference section of the paper.

Supplementary information is available. See DOI: **https://doi.org/10.1039/d5ma00359h**

Acknowledgements

A. N., A. F. and O. G. acknowledge financial support from the project "Tech4You - Technologies for climate change adaptation and quality of life improvement" - ECS00000009, in the framework of PIANO NAZIONALE DI RIPRESA E RESILIENZA (PNRR). The authors acknowledge Dr I. D. Perrotta for her precious support in the TEM analysis. The authors acknowledge Dr A. Bozzarello for his administrative support and management of the project.

References

1 G. Adamo, S. Campora and G. Ghersi, *Nanostructures for Novel Therapy*, ed. D. Ficai and A. M. Grumezescu, Elsevier, 2017, pp. 57–80.
2 D. R. Amin, C. Sugnaux, K. H. A. Lau and P. B. Messersmith, *Biomimetics*, 2017, **2**, 17.
3 T. Sugimoto, *J. Colloid Interface Sci.*, 2007, **309**, 106–118.
4 M. Danaei, M. Dehghankhold, S. Ataei, F. Hasanzadeh Davarani, R. Javanmard, A. Dokhani, S. Khorasani and M. R. Mozafari, *Pharmaceutics*, 2018, **10**, 57.
5 H. Coskun, A. Aljabour, L. Uiberlacker, M. Strobel, S. Hild, C. Cobet, D. Farka, P. Stadler and N. S. Sariciftci, *Thin Solid Films*, 2018, **645**, 320–325.
6 A. Olejnik, R. Bogdanowicz and J. Ryl, *J. Mol. Graphics Modell.*, 2025, **138**, 109045.
7 R. Mahata, S. Manna, M. Modak and S. M. Choudhury, *Med. Oncol.*, 2025, **42**, 165.
8 M. Gujrati, A. Malamas, T. Shin, E. Jin, Y. Sun and Z.-R. Lu, *Mol. Pharm.*, 2014, **11**, 2734–2744.
9 N. Joudeh and D. Linke, *J. Nanobiotechnol.*, 2022, **20**, 262.
10 L. A. Kolahalam, I. V. Kasi Viswanath, B. S. Diwakar, B. Govindh, V. Reddy and Y. L. N. Murthy, *Mater. Today: Proc.*, 2019, **18**, 2182–2190.
11 J. Subhra Sulipta, H. Jeong and S. Hong, *Biomater. Sci.*, 2025, **13**, 2261–2273.
12 S. Cai, Y. Cheng, C. Qiu, G. Liu and C. Chu, *Smart Mater. Med.*, 2023, **4**, 294–312.
13 V. N. Mochalin, O. Shenderova, D. Ho and Y. Gogotsi, *Nat. Nanotech.*, 2012, **7**, 11–23.
14 J. Ahlawat, S. M. Asil, G. G. Barroso, M. Nurunnabi and M. Narayan, *Biomater. Sci.*, 2021, **9**, 626–644.
15 O. Pop-Georgievski, N. Neykova, V. Proks, J. Houdkova, E. Ukraintsev, J. Zemek, A. Kromka and F. Rypaček, *Thin Solid Films*, 2013, **543**, 180–186.
16 P. Yang, Z. Gu, F. Zhu and Y. Li, *CCS Chem.*, 2020, **2**, 128–138.
17 J. Hu, L. Yang, P. Yang, S. Jiang, X. Liu and Y. Li, *Biomater. Sci.*, 2020, **8**, 4940–4950.
18 F. Mollica, R. Lucernati and R. Amorati, *J. Mater. Chem. B*, 2021, **9**, 9980–9988.
19 Y. Liu, K. Ai, J. Liu, M. Deng, Y. He and L. Lu, *Adv. Mater.*, 2013, **25**, 1353–1359.
20 D. Aguilar-Ferrer, T. Vasileiadis, I. Iatsunskyi, M. Ziółek, K. Żebrowska, O. Ivashchenko, P. Błaszkiewicz, B. Grześkowiak, R. Pazos, S. Moya, M. Bechelany and E. Coy, *Adv. Funct. Mater.*, 2023, **33**, 2304208.
21 S. H. Kim, S. M. Sharker, H. Lee, I. In, K. D. Lee and S. Y. Park, *RSC Adv.*, 2016, **6**, 61482–61491.
22 P. Yang, S. Zhang, X. Chen, X. Liu, Z. Wang and Y. Li, *Mater. Horiz.*, 2020, **7**, 746–761.
23 S. Gao, D. Zhang, M. Pedrero, Z. Guo, J. M. Pingarrón, S. Campuzano and X. Zou, *Coord. Chem. Rev.*, 2024, **501**, 215564.

24 Z. Qin, D. Li, Y. Ou, S. Du, Q. Jiao, J. Peng and P. Liu, *Crystals*, 2023, **13**, 976.
25 M. Suneetha, S. A. Alshehri and S. S. Han, *Colloids Surf., A*, 2025, **711**, 136354.
26 S. Acter, M. Moreau, R. Ivkov, A. Viswanathan and W. Ngwa, *Nanomaterials*, 2023, **13**, 1656.
27 A. Jin, Y. Wang, K. Lin and L. Jiang, *Bioact. Mater.*, 2020, **5**, 522–541.
28 I. Zmerli, J.-P. Michel and A. Makky, *Multifunct. Mater.*, 2021, **4**, 022001.
29 C. Huang, X. Wang, P. Yang, S. Shi, G. Duan, X. Liu and Y. Li, *Macromol. Rapid Commun.*, 2023, **44**, 2100916.
30 R. Djermane, C. Nieto, J. C. Vargas, M. Vega and E. M. Martín Del Valle, *Polym. Chem.*, 2022, **13**, 235–244.
31 C.-C. Ho and S.-J. Ding, *J. Mater. Sci.: Mater. Med.*, 2013, **24**, 2381–2390.
32 C.-T. Chen and M. J. Buehler, *Phys. Chem. Chem. Phys.*, 2018, **20**, 28135–28143.
33 C. Alonso, C. Nieto, J. C. Vargas, M. A. Vega and E. M. Martín del Valle, *Chem. Eng. J. Adv.*, 2024, **20**, 100638.
34 M. Wu, T. Wang, L. Müller and F. A. Müller, *Colloids Surf., A*, 2020, **603**, 125196.
35 Y. Liu, K. Ai and L. Lu, *Chem. Rev.*, 2014, **114**, 5057–5115.
36 P. Zhang, X. Li, Q. Xu, Y. Wang and J. Ji, *Colloids Surf., B*, 2021, **208**, 112125.
37 S. Sarkari, M. Khajehmohammadi, N. Davari, D. Li and B. Yu, *Front. Bioeng. Biotechnol.*, 2022, **10**, 1005413.
38 D. Wang, Q. Wang, Z. Lin, T. Pang and N. Ding, *Crystals*, 2023, **13**, 607.
39 V. Ball, *Front. Bioeng. Biotechnol.*, 2018, **6**, 109, DOI: **10.3389/fbioe.2018.00109**.
40 H. Xu, B. W. Zeiger and K. S. Suslick, *Chem. Soc. Rev.*, 2013, **42**, 2555–2567.
41 F. Liu, X. He, J. Zhang, H. Chen, H. Zhang and Z. Wang, *J. Mater. Chem. B*, 2015, **3**, 6731–6739.
42 F. Chen, Y. Xing, Z. Wang, X. Zheng, J. Zhang and K. Cai, *Langmuir*, 2016, **32**, 12119–12128.
43 T. Posati, M. Nocchetti, A. Kovtun, A. Donnadio, M. Zambianchi, A. Aluigi, M. L. Capobianco, F. Corticelli, V. Palermo, G. Ruani, R. Zamboni, M. L. Navacchia and M. Melucci, *ACS Omega*, 2019, **4**, 4839–4847.
44 J. C. García-Mayorga, H.-C. Rosu, A. B. Jasso-Salcedo and V. A. Escobar-Barrios, *RSC Adv.*, 2023, **13**, 5081–5095.
45 N. F. Della Vecchia, A. Luchini, A. Napolitano, G. D'Errico, G. Vitiello, N. Szekely, M. d'Ischia and L. Paduano, *Langmuir*, 2014, **30**, 9811–9818.
46 W. Zheng, H. Fan, L. Wang and Z. Jin, *Langmuir*, 2015, **31**, 11671–11677.
47 H. Liu, X. Qu, H. Tan, J. Song, M. Lei, E. Kim, G. F. Payne and C. Liu, *Acta Biomater.*, 2019, **88**, 181–196.
48 B. H. Stuart, *Infrared Spectroscopy: Fundamentals and Applications*, John Wiley & Sons, 2004.
49 S. Roy and J.-W. Rhim, *Colloids Surf., B*, 2019, **176**, 317–324.
50 E. Coy, I. Iatsunskyi, J. C. Colmenares, Y. Kim and R. Mrówczyński, *ACS Appl. Mater. Interfaces*, 2021, **13**, 23113–23120.
51 M. T. Cortés, C. Vargas, D. A. Blanco, I. D. Quinchanegua, C. Cortés and A. M. Jaramillo, *J. Chem. Educ.*, 2019, **96**, 1250–1255.
52 X. Yu, H. Fan, Y. Liu, Z. Shi and Z. Jin, *Langmuir*, 2014, **30**, 5497–5505.
53 A. C. Ferrari, *Solid State Commun.*, 2007, **143**, 47–57.
54 K. Lee, M. Park, K. G. Malollari, J. Shin, S. M. Winkler, Y. Zheng, J. H. Park, C. P. Grigoropoulos and P. B. Messersmith, *Nat. Commun.*, 2020, **11**, 4848.
55 R. Tejido-Rastrilla, G. Baldi and A. R. Boccaccini, *Ceram. Int.*, 2018, **44**, 16083–16087.
56 H. Takeuchi and I. Harada, *Spectrochim. Acta, Part A*, 1986, **42**, 1069–1078.
57 D. Renard, S. Tian, A. Ahmadivand, C. J. DeSantis, B. D. Clark, P. Nordlander and N. J. Halas, *ACS Nano*, 2019, **13**, 3117–3124.
58 A. J. Steeves and F. Variola, *J. Mater. Chem. B*, 2020, **8**, 199–215.
59 J. Feng, H. Fan, D. Zha, L. Wang and Z. Jin, *Langmuir*, 2016, **32**, 10377–10386.
60 I. Badillo-Ramírez, J. M. Saniger, J. Popp and D. Cialla-May, *Phys. Chem. Chem. Phys.*, 2021, **23**, 12158–12170.
61 M. Spracklin, DOI: **10.20381/RUOR-27517**.
62 M. Kim, K. K. Leong, N. Amiralian, Y. Bando, T. Ahamad, S. M. Alshehri and Y. Yamauchi, *Appl. Phys. Rev.*, 2024, **11**, 041317.
63 S. Roy, L. Van Hai, H. C. Kim, L. Zhai and J. Kim, *Carbohydr. Polym.*, 2020, **231**, 115729.
64 M. Xiao, M. D. Shawkey and A. Dhinojwala, *Adv. Opt. Mater.*, 2020, **8**, 2000932.
65 N. M. El Ghoubary, M. Fadel and D. A. A. Fadeel, *J. Basic Appl. Sci.*, 2023, **12**, 13.
66 A. Menichetti, D. Mordini and M. Montalti, *Int. J. Mol. Sci.*, 2024, **25**, 8975.
67 Y. Hu, H. Sun and T. Mu, *Int. J. Food Sci. Technol.*, 2023, **58**, 4715–4725.
68 X. Huang, P. K. Jain, I. H. El-Sayed and M. A. El-Sayed, *Nanomedicine*, 2007, **2**, 681–693.
69 Q. Chen, C. Wang, L. Cheng, W. He, Z. Cheng and Z. Liu, *Biomaterials*, 2014, **35**, 2915–2923.
70 K. Yang, S. Zhang, G. Zhang, X. Sun, S.-T. Lee and Z. Liu, *Nano Lett.*, 2010, **10**, 3318–3323.
71 J. Szewczyk, V. Babacic, A. Krysztofik, O. Ivashchenko, M. Pochylski, R. Pietrzak, J. Gapiński, B. Graczykowski, M. Bechelany and E. Coy, *ACS Appl. Mater. Interfaces*, 2023, **15**, 36922–36935.
72 Y. Liu, K. Ai, J. Liu, M. Deng, Y. He and L. Lu, *Adv. Mater.*, 2013, **25**, 1353–1359.